

Topological semimetal in a fermionic optical lattice

Kai Sun,¹ W. Vincent Liu ^{*,2,3,4} Andreas Hemmerich,⁵ and S. Das Sarma¹

¹Condensed Matter Theory Center and Joint Quantum Institute,

Department of Physics, University of Maryland, College Park, MD 20742, USA

²Department of Physics and Astronomy, University of Pittsburgh, Pittsburgh, PA 15260, USA

³Kavli Institute for Theoretical Physics, University of California, Santa Barbara, CA 93106, USA

⁴Center for Cold Atom Physics, Chinese Academy of Sciences, Wuhan 430071, China

⁵Institut für Laser-Physik, Universität Hamburg, Luruper Chaussee 149, 22761 Hamburg, Germany

Optical lattices play a versatile role in advancing our understanding of correlated quantum matter. The recent implementation of orbital degrees of freedom in checkerboard [1, 2] and hexagonal [3] optical lattices opens up a new thrust towards discovering novel quantum states of matter, which have no prior analogs in solid state electronic materials. Here, we demonstrate that an exotic topological semimetal emerges as a parity-protected gapless state in the orbital bands of a two-dimensional fermionic optical lattice. The new quantum state is characterized by a parabolic band-degeneracy point with Berry flux 2π , in sharp contrast to the π flux of Dirac points as in graphene. We prove that the appearance of this topological liquid is universal for all lattices with D_4 point group symmetry as long as orbitals with opposite parities hybridize strongly with each other and the band degeneracy is protected by odd parity. Turning on interparticle repulsive interactions, the system undergoes a phase transition to a topological insulator whose experimental signature includes chiral gapless domain-wall modes, reminiscent of quantum Hall edge states.

The search for topological states of matter has been a focus of theoretical and experimental studies, since the discovery of the quantum Hall effect (See the review of Ref. [4] and references therein). This problem was brought to the forefront again recently by the theoretical prediction and experimental discovery of the time-reversal invariant Z_2 topological insulators in semiconductors with strong spin-orbit couplings [5–11]. (For more details see the recent reviews of Refs. [12, 13] and references therein). For noninteracting particles, the topological properties of insulators as well as topological superconductors have recently been classified based on the anti-unitary symmetries of the systems [14, 15]. However, this elegant topological classification does not apply to Fermi liquid (metal or semimetal) states due to the existence of fermionic low-energy modes in gapless systems. In this paper, we shall show, however, that a novel type of topologically-nontrivial semimetal un-

expectedly arises as a universality class for arbitrary two-dimensional lattices with D_4 point group symmetry due to the mixing of orbitals of opposite parity. We believe that our discovery should be realizable in fermionic cold atom optical lattices rather easily.

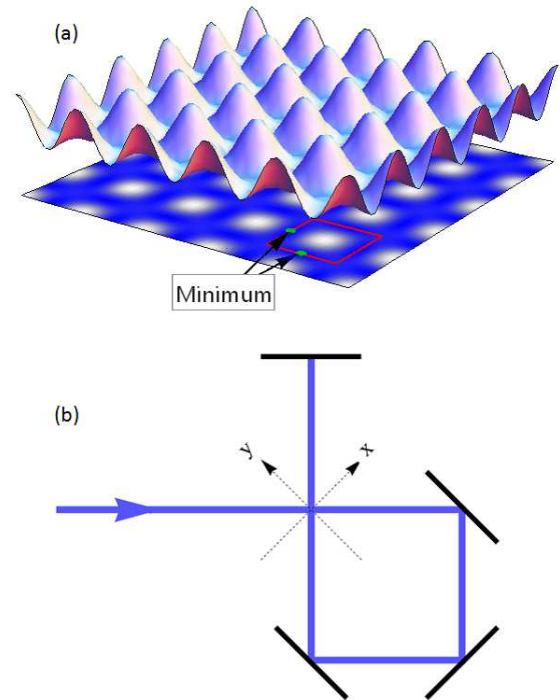


FIG. 1: (a) The optical lattice potential in equation (1). Here we choose $V_1 = 2.4E_R$ and $V_2 = 1.6E_R$, where $E_R = \hbar^2/(2m\lambda^2) = \hbar^2/(4ma^2)$ is the recoil energy with \hbar being the Planck constant, m being the mass of the particle, λ being the wavelength of the light beam and a being the lattice constant. The plane at the bottom shows the contour plot of the same potential. The red square marks an unit cell and the green dots indicate the two energy-minimum points of this unit cell located at the bond centers. (b) The experimental setup to realize the lattice potential in equation (1) for $V_2/V_1 \geq 1/2$. The linear polarization of the incident monochromatic light beam (solid blue line) encloses an angle α with respect to the normal direction to the drawing plane. The black bars represent mirrors and the dashed arrows mark the x and y directions of the coordinates. See Methods for analysis.

*email: w.vincent.liu@gmail.com.

The physics of higher orbitals in optical lattices has

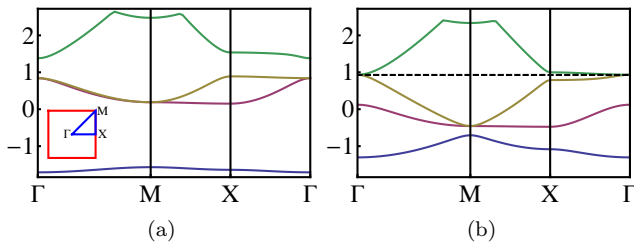


FIG. 2: The single-particle energy spectrum (measured in the unit of E_R) for the lowest four bands and the topological structure near band degeneracy points. (a) and (b) show the band structure for the momenta along the contour from Γ to M to X and back to Γ . This contour is shown in the inset in (a) represented by the blue lines, while the red square marks the Brillouin zone. At $V_1 = 2.4E_R$, two different types of band structures are observed. (a) shows the band structure at $V_2 < 0.87E_R$ ($V_2 = 0.4E_R$), where the hybridization between different orbitals is weak. We refer to this type of band structure as the weak-hybridization limit. The band structure at larger V_2 was shown in (b) with $V_2 = 1.6E_R$. This case is referred to as the strong-hybridization limit. The dashed line in (b) marks the chemical potential, at which the system becomes a topological semimetal. The marginal case $V_2 = 0.87E_R$ is shown in the Supplementary Information, where all the three upper bands touch at Γ point.

recently emerged as an exciting new front in both theoretical [16–18] and experimental (e.g., early [19–22] and recent [1–3]) studies. We specifically examine a model system that resembles the D_4 symmetric double-well lattice reported by the Hamburg experimental group [1, 2], but our conclusions apply generally to other lattices with the same point group symmetry. Consider the optical lattice shown in Fig. 1a with the potential

$$V(x, y) = -V_1[\cos(kx) + \cos(ky)] + V_2[\cos(kx + ky) + \cos(kx - ky)]. \quad (1)$$

Here, $k = 2\pi/a$ and a is the lattice constant. x and y are the 2D coordinates in configuration space. The parameters V_1 and V_2 are chosen to be positive. This optical lattice can be formed using a single chromatic light field following the experimental setup shown in Fig. 1b for $V_2/V_1 \geq 1/2$. For completeness, below we will first consider the general situation with $V_2/V_1 \geq 0$. Then, we will show that the parameter range of interest in our work is $V_2/V_1 \sim 2/3 > 1/2$, which can be realized using the proposed experimental setup shown in Fig. 1b and discussed below in the Methods section.

For $V_2 = 0$, the V_1 term induces a square lattice with lattice constant a . As V_2 increases, the potential energy at the center of a unit cell [with coordinates $(0, 0)$] is increased while the potentials near the bond centers [with coordinates $(\pm a/2, 0)$ and $(0, \pm a/2)$] are reduced. For $V_2 > V_1/2$, each unit cell contains potential minima located at $(\pm a/2, 0)$ and $(0, \pm a/2)$ as shown in Fig. 1a.

We numerically solve the band structure of this lattice via plan-wave expansions and find that band degeneracy

points appear between higher orbital bands at Γ and M points (the center and corner of the Brillouin zone). For the lowest four bands, as shown in Fig. 2, in the small V_2 limit, the second and third bands cross at both Γ and M points. For larger V_2 , there are still two band degeneracy points for the lowest four bands, but now the second and third bands only cross at M , while the third and fourth bands become degenerate at Γ . For even larger V_2 (not shown), the first and second bands become degenerate at M , while the third and fourth bands touch at Γ . This large V_2 limit is dominated by the same physics as in the intermediate V_2 regime, and thus, we will only focus on the small and intermediate V_2 in this paper.

The band degeneracy phenomenon described above is generic and stable. In fact, as shown in the Supplementary Information, for noninteracting particles, these band degeneracy points are topologically protected and remain stable when system parameters are tuned adiabatically, as long as the lattice point group symmetry is maintained (although a band degeneracy point may move from between the n and $n+1$ bands to the m and $m+1$ bands as shown in the examples above). With details presented in Methods and the Supplementary Information, near the band degeneracy point, a 2D vector field ($\vec{h}_{\vec{k}}$) in momentum space can be defined using the Hamiltonian of the system. At the momentum \vec{k} , the length of this 2D vector ($|\vec{h}_{\vec{k}}|$) gives (half of) the energy splitting between two energy bands. For the band degeneracy points in our model, this vector field possesses a topological defect, a vortex with winding number 2. At the vortex core, the length of the vector vanishes ($|\vec{h}_{\vec{k}}| = 0$), indicating that the band gap vanishes here (i.e., a band degeneracy point). It is this topological property that dictates the stability of the band degeneracy against any adiabatic deformation. From the mathematical point of view, this nontrivial topology can be described rigorously using the topological index of the Berry flux, which is 2π for this case.

In addition, the band degeneracy point is also protected by the parity of the Bloch wavefunctions under space inversion. In fact, as shown in the Methods section, it turns out that all the essential physics of the topological semimetal can be understood within a simple tight-binding picture without considering the full band structure theory, and the key ingredient for this phenomenon is the mixing between the orbitals of opposite parity. In the particular model we consider here, the semimetal is formed by the hybridization between the d orbital and the two p (p_x and p_y) orbitals at each lattice site.

We now study the instability of the topological semimetal in the presence of interaction, with details presented in Supplementary Information. We start with the tight-binding Hamiltonian and derive an effective low-energy theory around the Fermi point, which in this case is the degeneracy point of the third and fourth band (Fig. 2b). It turns out that this effective theory in the presence of interaction can be mapped onto a general theoretical model of d -wave symmetry which was analyzed

in Refs. [23, 24] via the renormalization group technique. Therefore, by mapping the results back from that d -wave model, we obtain the universal property for the band degeneracy point of the topological semimetal we present here. Below, we summarize the main results.

As temperature is lowered below a critical value, T_c , the system undergoes a second order phase transition, where $T_c \sim W e^{-\alpha/N(0)V}$ with $N(0)$ the density of states at the chemical potential, V the interaction strength and W the band width. The parameter α is a dimensionless constant whose value is determined by the band structure. In our model, the order parameter describing this low-temperature ordered phase is the z -component of the angular momentum $\langle L_{\vec{r}}^z \rangle = -i \langle p_{x,\vec{r}}^\dagger p_{y,\vec{r}} - p_{y,\vec{r}}^\dagger p_{x,\vec{r}} \rangle$, where $p_{x,\vec{r}}$ and $p_{y,\vec{r}}$ are the fermion annihilation operators of the p_x and p_y orbitals on site \vec{r} . (This order parameter can be mapped to the order parameter Φ in the general theory studied in Ref [23].)

In our system, the repulsive interaction can be reformulated as

$$H_{\text{int}} = V \sum_{\vec{r}} p_{x,\vec{r}}^\dagger p_{x,\vec{r}} p_{y,\vec{r}}^\dagger p_{y,\vec{r}} = -\frac{V}{2} \sum_{\vec{r}} (L_{\vec{r}}^z)^2, \quad (2)$$

where $V > 0$ is the interaction strength. This interaction term favors a state with nonzero angular-momentum $\langle L^z \rangle \neq 0$. In an ordinary metal or insulator (or graphene [25]), the formation of nonzero angular momentum costs kinetic energy which usually dominates over the energy gain from interaction unless the interaction strength is very large. However, for the topological semimetal we find here, the energy cost for nonzero L^z from the kinetic part is always subleading compared with the energy gain from interaction at low enough temperature. This results in the spontaneous generation of angular momentum, which is a key theoretical insight of our work.

From the symmetry point of view, this low temperature phase spontaneously breaks the D_4 point group symmetry down to C_4 , and also breaks the time-reversal symmetry. This symmetry breaking pattern belongs to the Ising universality class resulting in two degenerate ground states with opposite angular momentum.

As for the band structure, the band degeneracy at Γ is lifted in the symmetry broken phase. (The degeneracy at M is also lifted. However, this is not relevant to our study since that degeneracy point is located far below the chemical potential.) Hence the topological semimetal becomes a fully gapped insulator in the presence of interaction with the gap being $V\langle L^z \rangle$.

This insulator turns out to be topologically nontrivial characterized by the nontrivial value of the topological index, known as the first Chern number. The Chern number for this state is 1, which indicates that this system shares the same topological properties as the quantum Hall state with filling 1. However, in contrast to the quantum Hall effect where the nontrivial topological state is induced by a strong external magnetic field, here the same quantum topological state of matter originates from many-body effects in the absence of any ex-

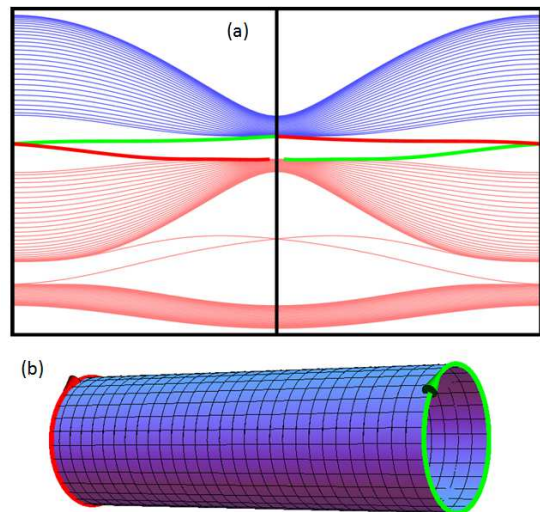


FIG. 3: Topologically protected edge states and domain-wall modes. Figure (a) shows the single-particle energy spectrum of the insulating phase with $\langle L^z \rangle \neq 0$ computed within mean-field approximation on a cylinder geometry (see Supplementary Information for technical details). The horizontal axis is the momentum defined along the periodical direction of the cylinder (from $-\pi/a$ to π/a) and the vertical axis is the energy. The pink curves at the bottom of (a) describes the states in the valence bands filled by particles, while the blue curves on the top part are the empty band. The green and red curves are the chiral gapless edge states located on the two edges of the cylinder as shown in (b). Here, figure (b) is a schematic picture showing the geometry of the system we used to compute the edge states. The black solid lines show the underlying square lattice. The two thick lines at the edges (red and green) represent the chiral edge states, with arrows indicating the chirality. The length of the cylinder we used is $30a$ with a being the lattice spacing. In this case, the finite-size effects are negligibly small.

ternal magnetic field. In general, states with nonzero Chern number in the absence of an external magnetic field are known as the anomalous quantum effect states, first proposed in a toy model on a honeycomb lattice by Haldane [26]. Recently, several different possible realizations of the Haldane model in cold gases were discussed using lattice rotations [27] or light-induced vector potentials [28]. In our predicted topological phase, however, interaction plays a decisive role in sharp contrast to the noninteracting situation prevailing in the quantum Hall effect or anomalous quantum Hall effect. To the best of our knowledge, our work is the only theoretical prediction in the literature of an interaction-driven anomalous quantum Hall state.

Furthermore, if two spin components are both present in the atomic gases, the same interaction effect may lead to a time-reversal invariant Z_2 topological insulator. This phenomenon can be partially understood as an interaction-driven 2D-version of HgTe. As pointed out in

Ref. [8], the combined effect of spin-orbit coupling and strain opens a gap at a 3D quadratic band degeneracy point and leads to a 3D topological insulator. By contrast, in our 2D system, topological states arise purely due to many-body interaction effects.

To further demonstrate the topological nature of this insulating phase, we computed the band structure of this state on a cylinder, as shown in Fig. 3. Here, although the bulk modes are all gapped, there is a gapless topological chiral edge state on each of the two edges of the system, which is the direct signature of a topologically nontrivial insulator.

The phase transition being discussed in our work has strong analogy to the BCS theory of superconductivity. In particular, the two classes have similar scaling formula for the mean-field transition temperature ($T_C \sim e^{\alpha/N(0)V}$). However, the phase transition here breaks only a discrete symmetry (time-reversal) and thus belongs to the Ising universality class. In 2D, the fluctuation effect is weak for an Ising transition and long-range order is sustained at finite temperature. On the contrary, the BCS transition breaks the continuous $U(1)$ symmetry and belongs to the XY universality class. As a result, the BCS transition in 2D is a Kosterlitz-Thouless transition, whose transition temperature is strongly suppressed by phase fluctuations and is much lower than the mean-field prediction. Thus the transition temperature for our problem should be much higher than the BCS transition, if all other parameters ($N(0)$, V , etc.) have the same value. Therefore, under equivalent conditions the phase transition predicted by us should be much easier to observe in 2D optical lattices than the corresponding BCS Kosterlitz-Thouless transition.

Beyond its theoretical significance, the topological semimetal state also has robust and unique experimental signatures. For example, the energy band structure of the unique band-crossing degeneracy point can be detected directly using experimental techniques, such as Bragg scattering [29] as discussed in our Supplementary Information.

At low temperatures, the system remains a topological semimetal for attractive interactions but becomes an insulator for repulsive interactions. Since both the values and the signs of interaction can be tuned in ultracold gases, this phase transition, between a compressible liquid and an incompressible insulator, can be studied experimentally by measuring the compressibility at different interactions. In addition, Bragg scattering can also be used to detect the insulating gap induced by the repulsive interactions. Because the low-temperature topological insulating state spontaneously breaks the time-reversal symmetry, any experimental measurements sensitive to the time-reversal symmetry can also be used to identify this phase, such as the Hall effect.

The direct experimental evidence for a topological insulator is the gapless chiral edge state which is a metallic state localized on the edge of a topologically-nontrivial insulator. However, it is worthwhile to note that the

sharp edge in the condensed matter system is absent in cold atomic gases. Due to the existence of the slowly varying trap potential, one expects the density to decrease away from the center of the trap. Therefore, the system is a liquid near the edge due to the low filling fraction. This liquid state from incommensurate filling will hybridize with the topological edge state, which makes the observation of the topological edge states challenging in atomic systems. This difficulty can be avoided if two domains of topological insulating phases with opposite angular momenta are induced. At the domain wall between these two areas, compressible chiral domain-wall states should exist. Since this domain wall can be chosen to locate near the center of the trap, far away from the trivial liquid state near the edge of the system, it should in principle provide a clean signature for the topological edge states. These domain-wall modes can also be detected using Bragg scattering, where one finds that the insulating gap is reduced to zero near the domain-wall. In each real experimental system, due to finite number of particles on a particular optical lattice, the vanishing of the insulating gap at the domain wall is in fact prohibited by finite size effects. For topological insulators, such finite size effects have been systematically studied and the metallic edge states are found to be detectable even for a system with about 10 particles [30]. An alternative experimental way of seeing the topological edge state would be to have a sharp trap boundary, as in a square-well potential, which would suppress the hybridization between the trivial liquid phase and the edge topological state. In such a square-well trap, the topological edge state should manifest itself directly.

Methods

Creation of the optical lattice. In the experimental setup shown in Fig. 1b of the Letter, by superimposing two monochromatic optical standing waves oscillating in phase, we implement the electric field

$$E = \epsilon \begin{pmatrix} -\frac{1}{\sqrt{2}} \sin \alpha \\ \frac{1}{\sqrt{2}} \sin \alpha \\ \cos \alpha \end{pmatrix} \cos [k(x+y)/2] - \epsilon \begin{pmatrix} \frac{1}{\sqrt{2}} \sin \alpha \\ \frac{1}{\sqrt{2}} \sin \alpha \\ \cos \alpha \end{pmatrix} \cos [k(x-y)/2]. \quad (3)$$

The corresponding light shift potential is $U(x, y) = -\chi |E(x, y)|^2$ with χ denoting the real part of the polarizability. It is straight forward to check that this potential is identical to the potential we proposed in the letter, up to a trivial constant:

$$U(x, y) = -V_1 [\cos(kx) + \cos(ky)] + V_2 [\cos(kx + ky) + \cos(kx - ky)] - \chi \epsilon^2, \quad (4)$$

with

$$V_1 = -\chi\epsilon^2 \cos^2 \alpha, \quad (5)$$

$$V_2 = -\chi\epsilon^2/2. \quad (6)$$

By choosing blue detuning, i.e., $\chi < 0$, we obtain $V_1 > 0$ and $V_2 > 0$. When the polarization direction, α , is changed, the ratio V_2/V_1 can be tuned to any value above 1/2. For example, using fermionic potassium ^{40}K with a principle fluorescence line at 767nm, a standard green frequency-doubled Nd:YAG-laser (532 nm) would be a suitable light source for implementing the desired optical potential.

Hybridization between orbitals of opposite parity. It turns out that all the essential physics of the topological semimetal can be understood within a simple tight-binding picture and the key-ingredient for this phenomenon is the mixing between orbitals with opposite parities under space inversion. Here, we outline the main procedures and results of calculation for the mixing of parity even $d_{x^2-y^2}$ and odd p_x and p_y orbitals, and defer the details (e.g., model Hamiltonian, band structure, etc.) to the Supplementary Information (Section S-6). In this study, these three orbital bands are considered next to the chemical potential level and all other orbitals are assumed to be far separate from them (such that their effects can be dynamically ignored). When the mixing between the two types of orbitals is weak, the parity-odd orbitals form two bands, which cross each other at the Γ and M points, while the band formed by the parity-even orbitals show no degeneracy (similar to Fig. 2a which was obtained by numerical diagonalization). In contrast, as the mixing between different types of orbitals is enhanced, the three bands formed by these three orbitals hybridize together, and now the middle band crosses with both the other two bands, one at Γ and another at M , similar to Fig. 2b. In fact, the top three bands shown in Fig. 2 are mainly contributed by the p_x , p_y and d orbitals. In the Supplementary Information, a full comparison is provided between the band structure of the optical lattice model defined by the potential (1) and that of the effective three-orbital ($p_x, p_y, d_{x^2-y^2}$) tight-binding model.

Instability under infinitesimal repulsion. Using the conclusions from Ref. [23], we found that under renormalization group, the repulsive interaction shown in equation (2) is a marginally-relevant perturbation and it is also the only relevant perturbation for spinless fermions with short-range interactions. Therefore, at low temperature, this interaction term dominates the low-energy physics and will stabilize a state with nonzero angular momentum $\langle L^z \rangle \neq 0$. This state is a topological insulator with Chern number 1, in agreement with the general study shown in Ref. [23]. This conclusion is further verified in Fig. 3, where we examined the mean-field single-particle spectrum for a cylindrical geometry and observed the gapless chiral edge states.

Acknowledgment

We appreciate the very helpful discussions with L. Fu, C. L. Kane and X.-L. Qi. The work of K. S. and S. D. S. is supported by JQI-NSF-PFC, AFOSR-MURI, ARO-DARPA-OLE, and ARO-MURI. W.V.L. is supported by ARO (W911NF-07-1-0293) and ARO-DARPA-OLE (W911NF-07-1-0464). We thank the Kavli Institute for Theoretical Physics at UCSB for its hospitality where this research is supported in part by National Science Foundation Grant No. PHY05-51164.

Author Contributions

WVL, KS, and SDS planned the work. KS and WVL carried out most of the calculations with input from SDS. AH provided the experimental protocol. All authors contributed to the writing of the manuscript.

Author Information

The authors declare no competing financial interests. Correspondence and requests for material should be sent to w.vincent.liu@gmail.com. Supplementary information accompanies this paper.

-
- [1] Wirth, G., Ölschläger, M. & Hemmerich, A. Evidence for orbital superfluidity in the p-band of a bipartite optical square lattice. *Nature Physics* **7**, 147–153 (2011).
- [2] Ölschläger, M., Wirth, G. & Hemmerich, A. Unconventional superfluid order in the f band of a bipartite optical square lattice. *Phys. Rev. Lett.* **106**, 015302 (2011).
- [3] Soltan-Panahi, P., Lühmann, D.-S., Struck, J., Windpassinger, P. & Sengstock, K. Quantum phase transition to unconventional multi-orbital superfluidity in optical lattices (2010). Preprint at <http://arxiv.org/abs/1104.3456>.
- [4] Nayak, C., Simon, S. H., Stern, A., Freedman, M. & Das Sarma, S. Non-abelian anyons and topological quantum computation. *Rev. Mod. Phys.* **80**, 1083–1159 (2008).
- [5] Kane, C. & Mele, E. *Phys. Rev. Lett.* **95**, 146802 (2005).
- [6] Bernevig, B. A., Hughes, T. L. & Zhang, S.-C. Quantum Spin Hall Effect and Topological Phase Transition in HgTe Quantum Wells. *Science* **314**, 1757–1761 (2006).
- [7] König, M. *et al.* Quantum Spin Hall Insulator State in HgTe Quantum Wells. *Science* **318**, 766–770 (2007).
- [8] Fu, L. & Kane, C. L. Topological insulators with inversion symmetry. *Phys. Rev. B* **76**, 045302 (2007).
- [9] Moore, J. E. & Balents, L. Topological invariants of time-reversal-invariant band structures. *Phys. Rev. B* **75**, 121306 (2007).

- [10] Roy, R. Z_2 classification of quantum spin hall systems: An approach using time-reversal invariance. *Phys. Rev. B* **79**, 195321 (2009).
- [11] D. Hsieh, et. al. A topological dirac insulator in a quantum spin hall phase. *Nature* **452**, 970–974 (2008).
- [12] Hasan, M. Z. & Kane, C. L. Colloquium: Topological insulators. *Rev. Mod. Phys.* **82**, 3045–3067 (2010).
- [13] Qi, X.-L. & Zhang, S.-C. Topological insulators and superconductors (2010). *Rev Mod Phys* (in press), Preprint at <http://arxiv.org/abs/1008.2026>.
- [14] Kitaev, A. Periodic table for topological insulators and superconductors (2009). Preprint at <http://arxiv.org/abs/0901.2686>.
- [15] Schnyder, A. P., Ryu, S., Furusaki, A. & Ludwig, A. W. W. Classification of topological insulators and superconductors in three spatial dimensions. *Phys. Rev. B* **78**, 195125 (2008).
- [16] Isacsson, A. & Girvin, S. M. Multi-flavor bosonic Hubbard models in the first excited Bloch band of an optical lattice. *Phys. Rev. A* **72**, 053604 (2005).
- [17] Liu, W. V. & Wu, C. Atomic matter of non-zero momentum Bose-Einstein condensation and orbital current order. *Phys. Rev. A* **74**, 013607 (2006).
- [18] Kuklov, A. B. Unconventional strongly interacting Bose-Einstein condensates in optical lattices. *Phys. Rev. Lett.* **97**, 110405 (2006).
- [19] Köhl, M., Moritz, H., Stöferle, T., Günter, K. & Esslinger, T. Fermionic atoms in a three dimensional optical lattice: Observing Fermi surfaces, dynamics, and interactions. *Phys. Rev. Lett.* **94**, 080403 (2005).
- [20] Browaeys, A. *et al.* Transport of atoms in a quantum conveyor belt. *Phys. Rev. A* **72**, 053605 (2005).
- [21] Lee, P. J. *et al.* Sublattice addressing and spin-dependent motion of atoms in a double-well lattice. *Phys. Rev. Lett.* **99**, 020402 (2007).
- [22] Müller, T., Fölling, S., Widera, A. & Bloch, I. State preparation and dynamics of ultracold atoms in higher lattice orbitals. *Phys. Rev. Lett.* **99**, 200405 (2007).
- [23] Sun, K., Yao, H., Fradkin, E. & Kivelson, S. A. Topological insulators and nematic phases from spontaneous symmetry breaking in 2d fermi systems with a quadratic band crossing. *Phys. Rev. Lett.* **103**, 046811 (2009).
- [24] Sun, K. & Fradkin, E. Time-reversal symmetry breaking and spontaneous anomalous hall effect in fermi fluids. *Phys. Rev. B* **78**, 245122 (2008).
- [25] Das Sarma, S., Adam, S., Hwang, E. H. & Rossi, E. Electronic transport in two-dimensional graphene. *Rev. Mod. Phys.* **83**, 407–470 (2011).
- [26] Haldane, F. D. M. Model for a quantum hall effect without landau levels: Condensed-matter realization of the “parity anomaly”. *Phys. Rev. Lett.* **61**, 2015–2018 (1988).
- [27] Wu, C. Orbital analogue of the quantum anomalous hall effect in p -band systems. *Phys. Rev. Lett.* **101**, 186807 (2008).
- [28] Stanescu, T. D., Galitski, V. & Das Sarma, S. Topological states in two-dimensional optical lattices. *Phys. Rev. A* **82**, 013608 (2010).
- [29] Ernst, P. T. *et al.* Probing superfluids in optical lattices by momentum-resolved bragg spectroscopy. *Nature Physics* **6**, 56–61 (2010).
- [30] Varney, C. N., Sun, K., Rigol, M. & Galitski, V. Interaction effects and quantum phase transitions in topological insulators. *Phys. Rev. B* **82**, 115125 (2010).
- [31] Blount, E. I. In Seitz, F. & Turnbull, D. (eds.) *Solid State Physics*, vol. 13 (Academic, New York, 1962).
- [32] Haldane, F. D. M. Berry curvature on the fermi surface: Anomalous hall effect as a topological fermi-liquid property. *Phys. Rev. Lett.* **93**, 206602 (2004).

Supplementary Information

S-1. OPTICAL LATTICE

Figure S1 shows the optical lattice described by

$$V(x, y) = -V_1[\cos(kx) + \cos(ky)] + V_2[\cos(kx + ky) + \cos(kx - ky)]. \quad (\text{S1})$$

In Fig. S1b, we employed the same parameters used in the letter to derive the topological semimetal. For $V_2 < V_1/2$ [Fig. S1.(a)], the optical lattice is basically a simple square lattice with a single energy minimum in each unit cell located at the center. However, when $V_2 > V_1/2$ [Fig. S1.(b) and (c)], there are two energy minima in a unit cell, located at the bond-center. As for the marginal case $V_2 = V_1/2$ (not shown), the minimum of the potential is reached when x or y becomes $2n\pi/k$ with n being any integer.

S-2. PLANE-WAVE EXPANSIONS AND NUMERICAL CALCULATION OF THE BAND STRUCTURE

We expand the Bloch wavefunction in the basis of plane waves

$$\Psi_{\vec{k}}^n(\vec{r}) = \sum_{n,m} a_{n,m} e^{i(2\pi n/a+k_x)x+i(2\pi m/a+k_y)y}, \quad (\text{S2})$$

where $a_{n,m}$ are the complex coefficients with n and m being integers and $\vec{r} = (x, y)$ is the real-space coordinates. In the lattice Hamiltonian, the potential energy introduces hybridization between the plane-waves with different n and m . For the low-energy bands, the contributions from plane waves with large m and n are small. Thus, we ignore

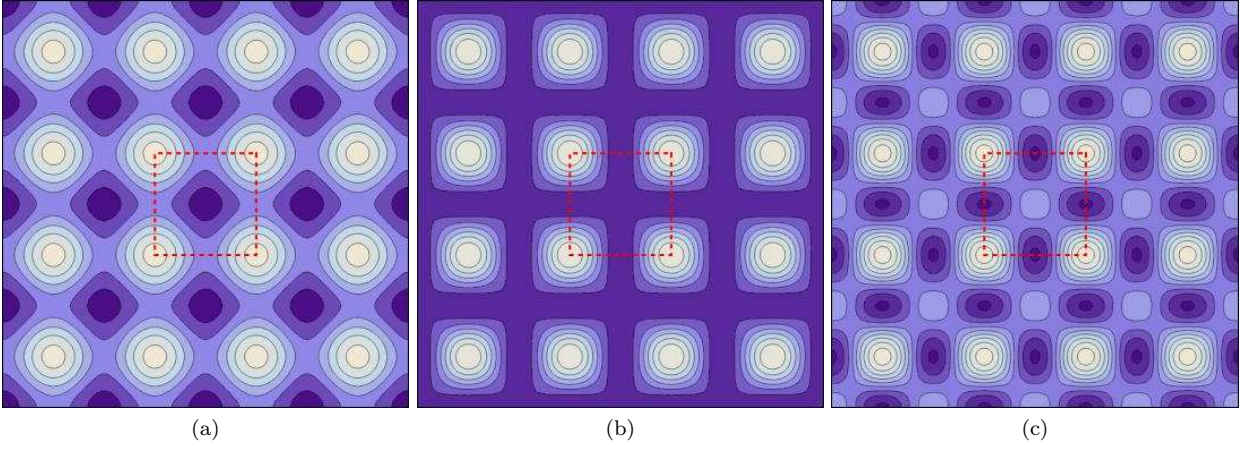


FIG. S1: The optical lattice shown in equation (S1) at different parameters. The darker (lighter) regions represent areas where the potential is low (high). The dashed line marks one unit cell of the lattice. In (a-c), $V_1 = 2.4E_R$ and $V_2 = 0.4E_R, 1.6E_R$ and $3.2E_R$.

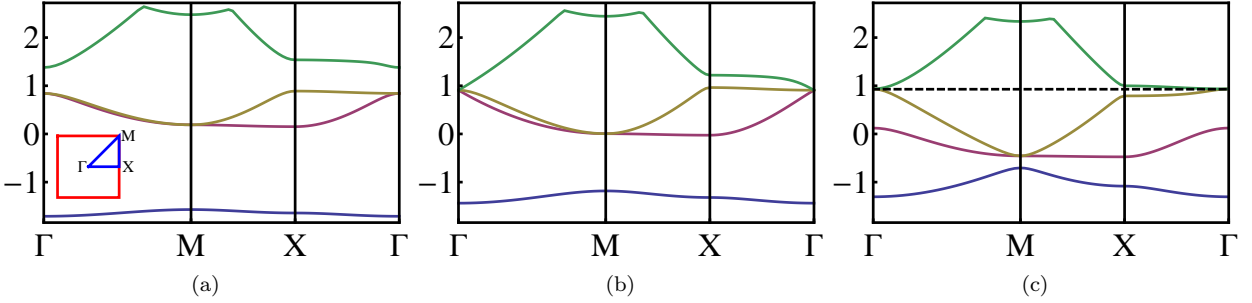


FIG. S2: The single-particle energy spectrum of the lowest four bands. Here, we show the band structure for the momenta along the contour from Γ to M to K and back to Γ , as shown in the inset of Fig. (a). The parameters here are chosen to be $V_1 = 2.4E_R$ while V_2 takes the value of (a) $0.4E_R$, (b) $0.87E_R$, and (c) $1.6E_R$, respectively.

states with n and m larger than certain cutoff N . In the numerical calculation demonstrated here, $N \sim 20$. And the band structure is independent of the choice of N for $N > 10$ (up to negligible small corrections to the eigenenergy.)

Using this approach, the Hamiltonian is a $(2N+1)^2 \times (2N+1)^2$ matrix. We find the eigenvalue and eigenvector of this matrix at each momentum in the Brillouin zone. The eigenvalues (as a function of \vec{k}) provides the single-particle band structure, while the eigenvector gives the coefficients of $a_{n,m}$ in equation (S2). In Fig. S2, the band structure is shown at $V_1 = 2.4E_R$ for different values of V_2 .

S-3. DEGENERACY OF PARITY ODD ORBITALS IN A POTENTIAL WELL WITH FOUR-FOLD ROTATIONAL SYMMETRY

Before studying the band degeneracy on a lattice, we examine the degeneracy of orbitals in a single potential well. The conclusions discovered here shall be generalized to the study of band degeneracy in the next section.

Consider a particle trapped in a 2D potential well with four-fold rotational symmetry. The symmetry group describing this rotational symmetry is the dihedral group of D_4 . We define $\phi^m(\vec{r})$ with $m = 1, 2, \dots$ to be the eigen-wavefunctions. Under a certain rotation in the symmetry group, $R \in D_4$, the wavefunctions $\phi^m(\vec{r})$ reads

$$\phi^n(\vec{r}) = \sum_m U_{n,m}(R) \phi^m(\vec{r}), \quad (\text{S3})$$

where $U_{n,m}(R)$ is the (n, m) element of the unitary matrix $U(R)$. By definition, the matrices $U(R)$ for all rotations in the point group forms a unitary representation of the symmetry group D_4 .

For any unitary representation of D_4 , it can always be separated into the direct sum of irreducible representations. In terms of the matrix $U(R)$, this means that it can be block diagonalized. Each block corresponds to an irreducible representation of D_4 . For a n -dimensional irreducible representation, the block has the size of $n \times n$.

In general, the states within a block (which belongs to the same irreducible representation of D_4) are related to each other via rotation. Since the system is invariant under D_4 , these states must have the same energy. Thus, for a state that belongs to an irreducible representation of dimensions $n > 1$, it must be n -fold degenerate.

For the D_4 group, there are 4 one-dimensional representations (known as A_1 , A_2 , B_1 and B_2) and 1 two-dimensional one (E). Interestingly, all the one-dimensional representations of D_4 are even under space-inversion

$$\phi^m(\vec{r}) = \phi^m(-\vec{r}). \quad (\text{S4})$$

On the other hand, the two-dimensional representation E has an odd parity

$$\phi^m(\vec{r}) = -\phi^m(-\vec{r}). \quad (\text{S5})$$

Therefore, we conclude that any space-inversion odd state in this system is two-fold degenerate, while space-inversion even states are in general nondegenerate.

S-4. SPACE-GROUP SYMMETRY AND BAND DEGENERACY POINTS

The crystal symmetries of a lattice are described by the corresponding space group G . Each element of the space group $\hat{g} = \{R|\vec{v}\}$ is a symmetry operation which combines a space rotation R (represented by a $d \times d$ orthogonal matrix with d being the spatial dimensions of the system) and a space translation \vec{v} (represented by a d -dimensional vector). For a spatial vector \vec{r} ,

$$\hat{g}\vec{r} = \{R|\vec{v}\}\vec{r} = R\vec{r} + \vec{v}. \quad (\text{S6})$$

The product of two group element is defined as

$$\hat{g}\hat{g}' = \{R|\vec{v}\}\{R'|\vec{v}'\} = \{RR'|\vec{v} + R\vec{v}'\}, \quad (\text{S7})$$

and the identity operator of the group is

$$\hat{e} = \{I|\vec{0}\}, \quad (\text{S8})$$

where I is the identity matrix and $\vec{0}$ is the vector with zero length.

The elements of the space group with $\vec{v} = \vec{0}$ forms a subgroup of G , which is the point group of the lattice. Another important subgroup is formed by the elements with $R = I$, which gives all the space translations commensurate with the lattice vector. By definition, equation (S7) implies that the space group is the semidirect product of the point group and the lattice translational group.

Consider the Bloch wavefunction $\Psi_{\vec{k}}^n(\vec{r})$, where n is the band index and \vec{k} is the momentum. Here we drop the spin index, which is irrelevant for our discussion. Under the transformation $\hat{g} = \{R|\vec{v}\}$, the Bloch wavefunction at momentum \vec{k} transfers into the Bloch wavefunction at momentum $R\vec{k}$:

$$\{R|\vec{v}\} : \Psi_{\vec{k}}^n(\vec{r}) \rightarrow \sum_m U_{\hat{g},\vec{k}}^{nm} \Psi_{R\vec{k}}^m(\vec{r}), \quad (\text{S9})$$

where $U_{\hat{g},\vec{k}}$ is a unitary matrix.

For each momentum \vec{k} , the rotations which keep \vec{k} invariant ($R\vec{k} = \vec{k}$) form a subgroup of the point group of the lattice. This subgroup is referred to as the little group $G_{\vec{k}}$. For the little group $G_{\vec{k}}$, equation (S9) reduces to

$$R\Psi_{\vec{k}}^n(\vec{r}) = \sum_m U_{R,\vec{k}}^{nm} \Psi_{\vec{k}}^m(\vec{r}). \quad (\text{S10})$$

Here the unitary matrices $U_{R,\vec{k}}$ form an unitary representation of the little group $G_{\vec{k}}$.

In a square lattice, the point group is D_4 . For the Γ point [$\vec{k} = (0,0)$] and the M point [$\vec{k} = (\pi/a, \pi/a)$], the little group coincides with the point group D_4 . Therefore, at any of these two momentum points, we can repeat the same

procedure as discussed in Sec. S-3. Similar conclusions are found concerning the phenomenon of the degeneracy. Namely, at the Γ or M point, if any of the Bloch waves is odd under space-inversion,

$$\Psi_{\vec{k}}^n(\vec{r}) = -\Psi_{\vec{k}}^n(-\vec{r}), \quad (\text{S11})$$

the states must be two-fold degenerate (i.e. two bands must cross at this momentum point). On the contrary, if the Bloch waves are even in parity,

$$\Psi_{\vec{k}}^n(\vec{r}) = \Psi_{\vec{k}}^n(-\vec{r}), \quad (\text{S12})$$

they are in general nondegenerate.

S-5. DEGENERACY AND PARITY OF ORBITALS

As shown above, the band degeneracy at Γ and M are determined by the parity of the Bloch wavefunctions under space inversion. Here we show that this parity can be deduced from the parity of the orbitals which form the energy band.

In the tight-binding picture, the orbitals at each site forms energy bands as tunnelings are introduced. Along this line of thinking, the Bloch wavefunction $\psi_{\vec{k}}^n(\vec{r})$ can be written as a superposition of local orbitals as:

$$\psi_{\vec{k}}^n(\vec{r}) = \frac{1}{\sqrt{N}} \sum_{\vec{R}, n} c_{n,m} \phi^m(\vec{r}) e^{i\vec{k} \cdot \vec{R}}, \quad (\text{S13})$$

where n is the band index and m indicates the orbitals on a single lattice site. $\phi^m(\vec{r})$ is the wavefunction for orbital m at certain site and $c_{n,m}$ is a complex coefficient. N in the normalization factor is the total number of sites of the lattice and \vec{R} gives the coordinate of the sites of the Bravais lattice.

Under the space inversion, I , we have

$$\vec{R} \rightarrow -\vec{R}, \quad (\text{S14})$$

$$\vec{r} \rightarrow -\vec{r}, \quad (\text{S15})$$

$$\vec{k} \rightarrow -\vec{k}. \quad (\text{S16})$$

At Γ and M , $e^{i\vec{k} \cdot \vec{R}} = \pm 1$ and thus is invariant. Therefore, as can be seen from equation (S13), the parity of a Bloch wavefunction at these two points is dictated by the parity of the orbitals that form this Bloch wave. In the particular case studied in the main text, the band formed by space-inversion odd orbitals are doubly degenerate at Γ and M . This will be demonstrated in details using a specific tight-binding model in Sec. S-6

S-6. HYBRIDIZATION BETWEEN ORBITALS OF OPPOSITE PARITY

A. Tight-binding model

Considering a square lattice with three orbitals on each site (p_x , p_y and $d_{x^2-y^2}$). The Hamiltonian of the tight-binding model takes the following form

$$\begin{aligned} H_0 = & -t_{dd} \sum_{\vec{r}} (d_{\vec{r}}^\dagger d_{\vec{r}+\vec{a}_x} + d_{\vec{r}}^\dagger d_{\vec{r}+\vec{a}_y} + h.c.) \\ & + t_{pp} \sum_{\vec{r}} (p_{x,\vec{r}+\vec{a}_x}^\dagger p_{x,\vec{r}} + p_{y,\vec{r}+\vec{a}_y}^\dagger p_{y,\vec{r}} + h.c.) - t'_{pp} \sum_{\vec{r}} (p_{x,\vec{r}+\vec{a}_y}^\dagger p_{x,\vec{r}} + p_{y,\vec{r}+\vec{a}_x}^\dagger p_{y,\vec{r}} + h.c.) \\ & + t_{pd} \sum_{\vec{r}} (p_{x,\vec{r}+\vec{a}_x}^\dagger d_{\vec{r}} - p_{x,\vec{r}}^\dagger d_{\vec{r}+\vec{a}_x} + p_{y,\vec{r}+\vec{a}_y}^\dagger d_{\vec{r}} - p_{y,\vec{r}}^\dagger d_{\vec{r}+\vec{a}_y} + h.c.) \\ & + \delta \sum_{\vec{r}} d_{\vec{r}}^\dagger d_{\vec{r}}, \end{aligned} \quad (\text{S17})$$

where \vec{r} is the coordinates of the lattice sites; \vec{a}_x (\vec{a}_y) is the lattice vector in the x (y) direction, and $p_{x,\vec{r}}$, $p_{y,\vec{r}}$ and $d_{\vec{r}}$ are the fermion annihilation operators for the p_x , p_y and $d_{x^2-y^2}$ orbitals at site \vec{r} . The hopping between orbitals on

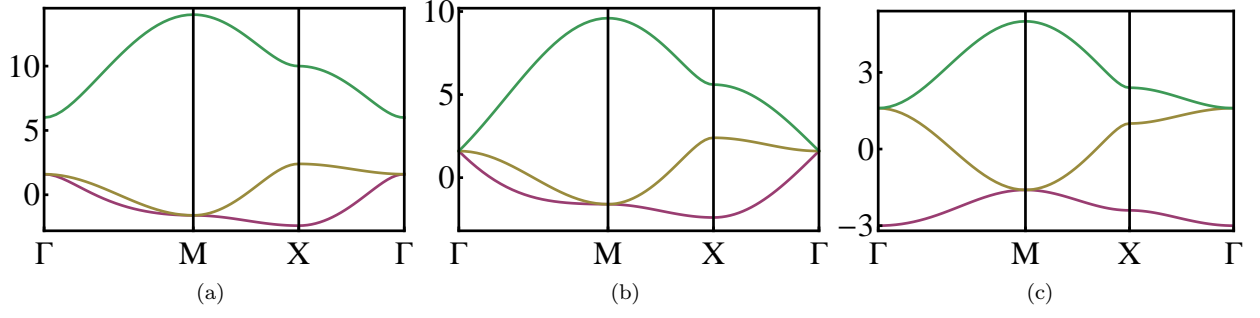


FIG. S3: The single-particle energy spectrum in the tight-binding model. The band structure of (a) is the weak-hybridization case, while (c) shows the strong-hybridization regime. The marginal case is shown in (b). Here, we choose the hopping strength $t_{dd} = t_{pp} = t_{pd} = 1$ and $t'_{pp} = 0.2$. From (a) to (c), the values of δ are 10, 5.6 and 1. The tight-binding model captures qualitatively the band structure of the second, third and fourth band shown in Fig. S2.

neighboring sites is described by the hopping amplitudes t_{dd} , t_{pp} , t_{pd} and t'_{pp} . The sign and strength of the hoppings are determined by the over-lap between orbitals. In our convention, all the hopping strengths here are positive and t'_{pp} is the smallest. The last term gives the energy difference between p and d orbitals for a single site problem δ , which we assume to be positive.

In the momentum space, the tight-binding Hamiltonian becomes

$$H_0 = \sum_{\vec{k}} \left(d_{\vec{k}}^\dagger, p_{x,\vec{k}}^\dagger, p_{y,\vec{k}}^\dagger \right) \mathcal{H} \begin{pmatrix} d_{\vec{k}} \\ p_{x,\vec{k}} \\ p_{y,\vec{k}} \end{pmatrix}, \quad (\text{S18})$$

where $d_{\vec{k}}$, $p_{x,\vec{k}}$ and $p_{y,\vec{k}}$ are the fermion annihilation operations at momentum \vec{k} and

$$\mathcal{H} = \begin{pmatrix} -2t_{dd}(\cos k_x + \cos k_y) + \delta & 2it_{pd} \sin k_x & 2it_{pd} \sin k_y \\ -2it_{pd} \sin k_x & 2t_{pp} \cos k_x - 2t'_{pp} \cos k_y & 0 \\ -2it_{pd} \sin k_x & 0 & 2t_{pp} \cos k_y - 2t'_{pp} \cos k_x \end{pmatrix}. \quad (\text{S19})$$

For simplicity, we choose the lattice constant $a = 1$.

The eigenvalues of the 3×3 matrix in equation (S19) gives the band structure. Depending on the value of δ (compared with the hopping strength), two different types of band structures are found as shown in Fig. S3. For $\delta > 4t_{dd} + 2t_{pp} - 2t'_{pp}$, the weak hybridization is observed, but for $\delta < 4t_{dd} + 2t_{pp} - 2t'_{pp}$ the strong-hybridization regime is reached. For the marginal case at $\delta = 4t_{dd} + 2t_{pp} - 2t'_{pp}$, the three bands touch at Γ . This recovers the band structure calculated from plan wave expansion for the optical lattice presented in the main text, if we identify these three bands as the second, third and fourth band there.

B. Generalization

It turns out that the conclusion above can be generalized to other orbitals of opposite parity. To demonstrate this, we consider a general tight-binding model on a square lattice. We further assume that at each site, only one parity even orbital and a pair of parity odd orbitals are close to the chemical potential, so that we can ignore all other orbitals in the leading order approximation. Here we consider two parity odd orbitals because for any potential wells with four-fold rotational symmetry, the odd parity orbitals are doubly degenerate, while the even parity orbitals are in general nondegenerate. We also assume the energy difference between of the parity-even and parity-odd orbitals is described by a parameter δ .

When δ is much larger than the hopping strength, the parity-even and parity-odd orbitals are separated in energy. Therefore, the mixing between these two types of orbitals is small. Roughly speaking, in this limit, the parity-even orbitals will form one band, which in general has no degeneracy point. The parity-odd orbitals form two bands, which cross each other at Γ and M , due to the odd parity of the orbitals. This is the weak strong-hybridization limit.

On the other hand, when δ is small compared with the hopping strength, the hybridization between parity-even and parity-odd becomes important. In this case, it is no longer possible to identify the distinct parity-even band and parity-odd bands, since all the three bands are now mixed together. Here, the upper two bands cross at Γ (or M) and the lower two bands cross at M (or Γ), which gives us the strong-hybridization limit.

S-7. TOPOLOGICAL PROTECTION OF THE BAND DEGENERACY POINTS

In this section we provide two equivalent topological indices to prove the topological nature of the band degeneracy. The first approach shows that the band degeneracy point can be considered as a vortex in the momentum space with integer winding numbers, and the second one presents the same topological structure through the concept of the Berry flux [31, 32].

A. Band degeneracy as a topological defect in momentum space

Consider the tight-binding model presented in equation (S18). Near the band degeneracy point at Γ , it is easy to check that the energy of the fermion modes from d orbitals are far away from the chemical potential, so we can integrate out these high-energy degrees of freedom and focus only on the low-energy modes (from p orbitals). By doing so, the Hamiltonian is reduced to an effective two-band model with

$$H_0 = \sum_{\vec{k}} \begin{pmatrix} p_{x,\vec{k}}^\dagger & p_{y,\vec{k}}^\dagger \end{pmatrix} \tilde{\mathcal{H}} \begin{pmatrix} p_{x,\vec{k}} \\ p_{y,\vec{k}} \end{pmatrix}. \quad (\text{S20})$$

Here, although the d orbitals drop off from the Hamiltonian, the kernel of the Hamiltonian, $\tilde{\mathcal{H}}$, receives corrections from virtual processes in which a particle jumps from a p orbital to a d orbital and then back to a p orbital (and other higher-order virtual processes, which we would not consider here). Using perturbation theory, the matrix $\tilde{\mathcal{H}}$ can be determined order-by-order as

$$\tilde{\mathcal{H}} = \begin{pmatrix} \mathcal{H}_{22} & \mathcal{H}_{23} \\ \mathcal{H}_{32} & \mathcal{H}_{33} \end{pmatrix} - \frac{1}{H_{11} - \mu} \begin{pmatrix} \mathcal{H}_{21}\mathcal{H}_{12} & \mathcal{H}_{21}\mathcal{H}_{13} \\ \mathcal{H}_{31}\mathcal{H}_{12} & \mathcal{H}_{31}\mathcal{H}_{13} \end{pmatrix} + \dots \quad (\text{S21})$$

where μ is the chemical potential and \mathcal{H}_{ij} is the (i, j) component of the matrix shown in equation (S19). Here, the first term on the right hand side is the zeroth order term in the perturbation expansion, generated by direct hoppings between p orbitals, while the second term is from the second order perturbation, which describes the virtual hopping processes mentioned above.

By expanding the momentum around the Γ point, to the leading order, equation (S20) becomes

$$H_0 = \sum_{\vec{k}} \begin{pmatrix} p_{x,\vec{k}}^\dagger & p_{y,\vec{k}}^\dagger \end{pmatrix} \begin{pmatrix} t_1 k_x^2 + t_2 k_y^2 & 2t_3 k_x k_y \\ 2t_3 k_x k_y & t_1 k_y^2 + t_2 k_x^2 \end{pmatrix} \begin{pmatrix} p_{x,\vec{k}} \\ p_{y,\vec{k}} \end{pmatrix}, \quad (\text{S22})$$

where

$$t_1 = t_{pp} + \frac{4t_{pd}^2}{2t_{pp} - 2t'_{pp} + 4t_{dd} - \delta}, \quad (\text{S23})$$

$$t_2 = -t'_{pp}, \quad (\text{S24})$$

$$t_3 = \frac{2t_{pd}^2}{2t_{pp} - 2t'_{pp} + 4t_{dd} - \delta}. \quad (\text{S25})$$

This Hamiltonian recovers the general model of a quadratic-band crossing point studied in Ref. [23].

The 2×2 matrix in equation (S22) can be expanded in the basis of four independent matrices of $SU(2)$ algebra as follows

$$\mathcal{H} = \frac{t_1 + t_2}{2}(k_x^2 + k_y^2)I + 2t_3 k_x k_y \sigma_x + \frac{t_1 - t_2}{2}(k_x^2 - k_y^2)\sigma_z, \quad (\text{S26})$$

where σ_x and σ_z are the two Pauli matrices and I is the 2×2 identity matrix. We can define a 2D planar vector using the coefficients of the two Pauli matrices

$$\vec{h} = \left(2t_3 k_x k_y, \frac{t_1 - t_2}{2}(k_x^2 - k_y^2) \right). \quad (\text{S27})$$

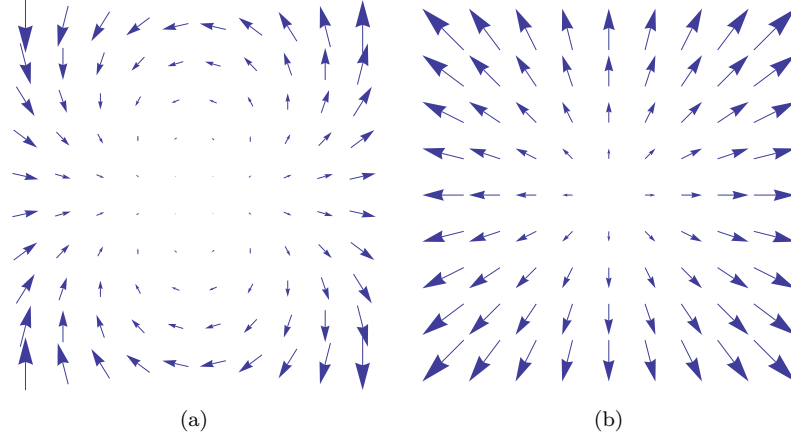


FIG. S4: Band degeneracy point as a topological defect. Here (a) shows the planar vector \vec{h} defined in equation (S27) in the momentum space near the band degeneracy point that we found in the square lattice model. For comparison, we show in (b) the same planar vector near the Dirac point as in graphene. In (c), we show that the band degeneracy point we found actually corresponds to a vortex in the momentum space with winding number 2. Here the vector field \mathcal{H} is defined in equation (S27). For comparison, we also show the same vector field for a Dirac point, which corresponds to a topological defect with winding number 1. This nontrivial winding number indicates that the band degeneracy is topologically protected and thus can not be lifted in adiabatic procedures, unless the symmetry of the system is broken.

The length of this vector $|\vec{h}|$ has the physical meaning of (half of) the band gap between the two bands, if one notice that the dispersion relation for the two bands are

$$E_{\pm} = \frac{t_1 + t_2}{2}(k_x^2 + k_y^2) \pm |\vec{h}|. \quad (\text{S28})$$

As shown in Fig. S4, this 2D planar vector \vec{h} has a vortex structure at $\vec{k} = 0$. A vortex is a topological defect described by the topological index (the winding number),

$$W = \oint_{\mathcal{C}} \frac{d\vec{k}}{2\pi} \cdot \left[\frac{h_x}{|\vec{h}|} \vec{\nabla} \left(\frac{h_y}{|\vec{h}|} \right) - \frac{h_y}{|\vec{h}|} \vec{\nabla} \left(\frac{h_x}{|\vec{h}|} \right) \right]. \quad (\text{S29})$$

For the topological semimetal which we consider here, the winding number is $W = 2$. For comparison, the vortex structure for a Dirac point is also plotted, which has winding number 1.

At the vortex core, $\vec{h} = 0$, which indicates a band degeneracy point. Thus, the band degeneracy can be considered as a topological defect in the momentum space. It is this topological nature that protects the band degeneracy that we have found from being lifted against any adiabatic deformation of the Hamiltonian.

In fact, this vortex structure is generic for symmetry protected band-degeneracy point. In general, if we focus on the two bands of the degeneracy point and treat the system as a two-band model, the Hamiltonian can always be expanded into the identity matrix and the Pauli matrices, as in equation (S26). In the presence of the time-reversal and space inversion symmetries, at most two Pauli matrices can appear while the third one is forbidden due to symmetry. Thus, we can use the coefficients of the two Pauli matrices to form a 2D planar vector as in equation (S27) and the length of this vector gives the band gap between the two bands.

B. Berry flux and degeneracy points

The same topological nature can be presented in terms of the Berry flux. The Berry flux is defined as the contour integral of the Berry connection in the momentum space [31, 32].

$$\Phi_B^n = \oint_{\mathcal{C}} d\vec{k} \cdot \vec{A}_{\vec{k}}^n, \quad (\text{S30})$$

where n is the band index and \mathcal{C} is certain closed contour in the momentum space. Here, the Berry connection $\vec{\mathcal{A}}_{\vec{k}}^n$ is defined as

$$\vec{\mathcal{A}}_{\vec{k}}^n = -i \int d^2r \Psi_{\vec{k}}^n(\vec{r})^* \vec{\nabla}_{\vec{r}} \Psi_{\vec{k}}^n(\vec{r}), \quad (\text{S31})$$

with $\Psi_{\vec{k}}^n(\vec{r})$ being the Bloch wave of band n at momentum \vec{k} . The Berry connection $\vec{\mathcal{A}}_{\vec{k}}^n$ can be roughly considered as a gauge field in the momentum space. In this analogy, the Berry flux corresponds to the magnetic flux in the area enclosed by contour \mathcal{C} . Similar as the flux quantization of the magnetic field, the Berry flux of a time-reversal invariant system is quantized to $m\pi$ with m being an integer [31, 32].

However, in the definition of the Bloch wavefunctions, there is an undetermined $U(1)$ phase that can be chosen arbitrarily. This can be seen by noticing that for any Bloch wave $\Psi_{\vec{k}}^n(\vec{r})$, the following equation,

$$\tilde{\Psi}_{\vec{k}}^n(\vec{r}) = e^{i\phi(\vec{k})} \Psi_{\vec{k}}^n(\vec{r}), \quad (\text{S32})$$

also defines a Bloch wave where $\phi(\vec{k})$ is an arbitrary function of momentum \vec{k} . For any $\phi(\vec{k})$, the integral over a closed contour \mathcal{C} in the BZ,

$$W = \oint_{\mathcal{C}} d\vec{k} \nabla_{\vec{k}} \phi(\vec{k}), \quad (\text{S33})$$

always leads to an integer value due to the periodical structure around the contour.

For a general contour \mathcal{C} , the redefinition of phase in equation (S32) changes the value of the Berry flux by $2W\pi$. Therefore, the Berry flux is only well defined up to mod 2π . Since the Berry flux is quantized to integer multiplied by π , only two classes of flux, $\Phi_B = 0$ and π , can be distinguished. All other values of Φ_B can be connected to these two classes via redefinition of phase in equation (S32).

However, for a system with space inversion symmetry, if the contour was also chosen in such a way that it is invariant under space inversion (i.e. if \vec{k} is a point on the contour, so is $-\vec{k}$), then the Berry flux can be defined up to mod 4π . This can be achieved by requiring

$$I\Psi_{\vec{k}}^n(\vec{r}) = \Psi_{-\vec{k}}^n(\vec{r}), \quad (\text{S34})$$

where I is the space-inversion operator. This is always possible by choosing a proper ϕ and redefine the Bloch waves as in equation (S32). With this constraint, the redefinition of phase [equation (S32)] can only be allowed for $\phi(\vec{k}) = 2n\pi + \phi(-\vec{k})$ with n being an integer. Therefore, the winding number W [equation (S33)] must be even, $W = 2m$ with m being an integer. Thus, the Berry flux will now change by $4m\pi$ under any phase redefinition. As a result, the Berry flux becomes well defined up to mod 4π . Opposite to the general case discussed above, now the Berry flux 2π and 0 are topologically distinguished states and cannot be adiabatically deformed into each other. This is one example where a discrete symmetry of the system (e.g. the point group symmetry) changes the topological classification of a system.

For the problem we study here, we can always choose the eigenvector [$a_{n,m}$ in equation (S2)] to be real. This enables the computation of the Berry flux via a simpler method. If one considers the phase uncertainty shown in equation (S32) as a gauge-like symmetry in the momentum space, this approach is in analogy to adopting a specific gauge which helps simplify the computation for physical quantities. We first require all the coefficients $a_{n,m}$ to be real. However, there is still an arbitrary sign undetermined for $a_{n,m}$ at each \vec{k} . To fix this sign, we choose a contour around the Γ or M point and require the wavefunction to satisfy the relation

$$\int [\Psi_{\vec{k}}^n(\vec{r})]^* \Psi_{\vec{k}'}^n(\vec{r}) d^2r = 1 + O(|\vec{k} - \vec{k}'|), \quad (\text{S35})$$

for any two momentums \vec{k} and \vec{k}' on the contour which are close to each other. Now, one still has the freedom to flip the sign for $a_{n,m}$ for all the points on the contour at the same time, but up to this sign, the value of $a_{n,m}$ is determined, which can be viewed as a gauge fixing.

Due to the space inversion symmetry, the coefficients $a_{n,m}$ at \vec{k} and $-\vec{k}$ must have the same amplitude but can have either the same or opposite signs:

$$a_{n,m}(\vec{k}) = a_{n,m}(-\vec{k}), \text{ or } a_{n,m}(\vec{k}) = -a_{n,m}(-\vec{k}). \quad (\text{S36})$$

The Berry flux is zero for the first case but 2π for the second.

In the definition of the Berry flux, one uses the Bloch wavefunction in a specific band, say n . Therefore, the contour integral is well defined, when there is no band degeneracy on the contour. On the one hand, if the area enclosed by the contour has no band degeneracy point inside, one can continuously deform (shrink) the contour into a point, which by definition has zero Berry flux. During this adiabatic deformation of the contour, every quantity should change in a continuous way. On the other hand, the Berry flux is quantized and cannot be tuned adiabatically. Therefore, the Berry flux must be invariant during this process. These arguments lead to the following conclusion: for any contours enclosing no band degeneracy points for the band n , the Berry flux of this band must be zero. Now to the contrary, if the Berry flux is nonzero, this contour must not be able to shrink adiabatically to a point. The only way this is possible is when there is a band degeneracy point enclosed by this contour. Thus we prove that a nonzero Berry flux is the sufficient condition to have a protected band degeneracy point.

We end the discussion about the topological nature of the band degeneracy by unifying the two topological indices that we have computed in this section. In fact, if one multiplies the winding number studied in Sec. S-7 A by π , it coincides with the Berry flux examined in Sec. S-7 B.

S-8. INSTABILITY INDUCED BY REPULSIVE INTERACTIONS

The low-energy effective theory we constructed in Sec. S-7 A [equation (S22)] can be mapped exactly to the general theory studied in Refs. [23, 24]. By mapping the results found in Ref. [23] back into our model, the interaction effect can be solved in the weak-coupling limit. Here we summarize the results from this mapping and provide a simple mean-field picture for understanding this results.

In the low-energy effective theory for fermions with two bands (but no spin), only one interaction term needs considering,

$$H_{\text{int}} = V \sum_{\vec{r}} p_{x,\vec{r}}^\dagger p_{x,\vec{r}} p_{y,\vec{r}}^\dagger p_{y,\vec{r}}. \quad (\text{S37})$$

Other (short-range) interaction terms involve derivatives and thus are irrelevant in the sense of renormalization group (RG). As shown in Ref. [23], at low temperature, this interaction is marginal at tree level under RG, while the one-loop RG calculation shows that this interaction is marginally relevant for $V > 0$ (repulsive) and marginally irrelevant with $V < 0$. This implies that when the temperature is lowered for this system, for particles with attractive interactions, the noninteracting band structure theory remains accurate in the low energy limit. However, if the interaction is repulsive, it leads to an instability once the temperature is below certain critical value T_C . It worth emphasizing that the scaling behavior here is very similar to the BCS theory in Fermi liquids, except that the instability shows opposite behavior regarding the sign of interaction. In the latter case, the system is unstable for attractive interactions, but remains stable for repulsive interactions.

The result of this instability is a state with spontaneously generated angular momentum. This can be seen if one notices that the interaction term in equation (S37) can be reformulated as

$$H_{\text{int}} = -\frac{V}{2} \sum_{\vec{r}} (L_{\vec{r}}^z)^2, \quad (\text{S38})$$

up to some unimportant constant where

$$L_{\vec{r}}^z = -i(p_{x,\vec{r}}^\dagger p_{y,\vec{r}} - p_{y,\vec{r}}^\dagger p_{x,\vec{r}}), \quad (\text{S39})$$

is the angular momentum in the z -direction at site \vec{r} . The physical meaning of $L_{\vec{r}}^z$ can be checked by noticing

$$L^z |p_x + ip_y\rangle = +|p_x + ip_y\rangle, \quad (\text{S40})$$

$$L^z |p_x - ip_y\rangle = -|p_x - ip_y\rangle. \quad (\text{S41})$$

Here we verify equation (S38) by expanding it using the fermion creation and annihilation operators:

$$H_{\text{int}} = -\frac{V}{2} \sum_{\vec{r}} (L_{\vec{r}}^z)^2 = \frac{V}{2} \sum_{\vec{r}} (p_{x,\vec{r}}^\dagger p_{y,\vec{r}} p_{x,\vec{r}}^\dagger p_{y,\vec{r}} - p_{x,\vec{r}}^\dagger p_{y,\vec{r}} p_{y,\vec{r}}^\dagger p_{x,\vec{r}} - p_{y,\vec{r}}^\dagger p_{x,\vec{r}} p_{x,\vec{r}}^\dagger p_{y,\vec{r}} + p_{y,\vec{r}}^\dagger p_{x,\vec{r}} p_{y,\vec{r}}^\dagger p_{x,\vec{r}}). \quad (\text{S42})$$

Notice that the first and last term on the right hand side vanish because $p_{x,\vec{r}}^\dagger p_{x,\vec{r}}^\dagger = p_{y,\vec{r}}^\dagger p_{y,\vec{r}}^\dagger = 0$. The two remaining terms recover exactly the equation (S37), with an extra constant term: $VN/2$ where N is the total particle number in the system.

From equation (S38), it is transparent that repulsive interaction favors $L^z \neq 0$. Since the repulsive interaction is marginally relevant, it shall dominate the low energy behavior of the system. Therefore, repulsive interaction shall result in the low-temperature instability towards a state with spontaneously generated angular momentum and $\langle L^z \rangle$ is the order parameter for this phase. The nonzero value of this order parameter indicates that the low-temperature ordered phase breaks spontaneously the time-reversal symmetry and also reduces the point group symmetry from D_4 down to C_2 . Due to this symmetry breaking, the band degeneracy is no longer symmetry protected, and a gap opens at the band point. As a result, the system turns into an insulator with a finite energy gap. This insulator has a nontrivial topological structure, with the first Chern number being 1. The topological properties of this state is the same as the quantum Hall state with filling 1, but it is induced by interaction and spontaneous symmetry breaking, instead of a magnetic field. An insulating state of this kind of topological properties is often referred to as the quantum anomalous Hall state. [26]

For larger V , although a Hartree-Fock treatment can still be performed, the mean-field approximation becomes invalid as the energy scale of interaction becomes comparable with the band width. Furthermore, the low-energy effective theory, which we obtained by starting from a noninteracting band structure and treating interactions as perturbations, is not expected to describe the properties of a system with strong interactions. In this limit, the behavior of the system becomes sensitive to the microscopic details.

We repeated the same mean-field calculation including the d -orbitals and all the conclusions above remains the same. As have been shown in Sec. S-6 and S-7, the energy of the d -orbitals are far from the Fermi level near the band degeneracy point and the degeneracy at Γ is between the two p -bands. Therefore, the interactions between d orbitals are not relevant for analyzing the instability of this level degeneracy point, and the same is true for interactions between p and d orbitals. The only relevant interaction term here is the repulsions between p orbitals, same as observed above in the two-band approximation. In the full three-band model, this interactions can be decoupled using the standard mean-field approximation as

$$H_{MF} = H_0 - V \sum_{\vec{r}} \langle L_{\vec{r}}^z \rangle L_{\vec{r}}^z + \frac{V}{2} \sum_{\vec{r}} (L_{\vec{r}}^z)^2 \quad (\text{S43})$$

where H_0 is the hopping part defined in Eq. (S19) and $\langle L_{\vec{r}}^z \rangle$ is the order parameter which are determined by minimizing the free energy. Same as the two-band model we computed above, this three-band model shows the same instability at infinitesimal $V > 0$. We compared other competing orders, such as nematic and density waves, and found that the topological insulating state is preferred. In the ordered phase with $\langle L_{\vec{r}}^z \rangle \neq 0$, we can use the mean-field Hamiltonian [Eq. (S43)] to compute the energy spectrum. By solving the energy spectrum on a cylindrical geometry, we observed the topological edge modes as shown in Fig. 3 of the letter.

S-9. DETECTING THE TOPOLOGICAL SEMIMETAL USING BRAGG SCATTERING

Here, we briefly describe the experimental signatures of a semimetal state with respect to the application of Bragg scattering. When two laser beams with different frequencies and wavevectors are used, the particles in the system can absorb a photon from one beam and emit a photon into the other beam. In this process, the momentum gained by a particle confined in a 2D plane is $\vec{\delta q} = \vec{k}_{||,1} - \vec{k}_{||,2}$, where $\vec{k}_{||,1}$ and $\vec{k}_{||,2}$ are the in-plan components of the wavevectors of the two laser beams. In addition, the energy of the particle will change by $\delta\omega = \omega_1 - \omega_2$ with ω_1 and ω_2 being the frequencies of the beams. While ω can be tuned by changing the frequency of the two laser beams, $\vec{\delta q}$ can be tuned independently via tilting the direction of the beams out of the 2D plane. Therefore, we can treat $\vec{\delta q}$ and $\delta\omega$ as two independent control parameters. At a given value of $\vec{\delta q}$, as shown in Fig. S5, Bragg scattering is only allowed when $\delta\omega$ exceeds a threshold $\delta\omega^*$. The curves of $\delta\omega^*$ as a function of $\vec{\delta q}$ carry direct information on the band structure. For the topological semimetal, $\delta\omega^*$ is a quadratic function of $\vec{\delta q}$ and vanishes at $\vec{\delta q} = 0$. On the contrary, $\delta\omega^* > 0$ for an insulator at any $\vec{\delta q}$, while $\delta\omega^* = 0$ for a range of $\vec{\delta q}$ in a metal.

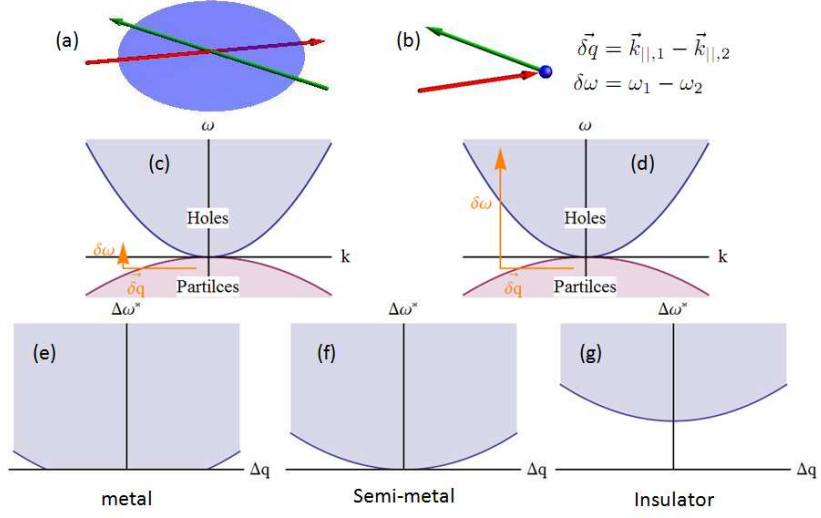


FIG. S5: Experimental signatures for the topological semimetal and topological insulator in Bragg scattering. On the top row, the experimental setup of Bragg scattering is shown in (a) and the schematic scattering process is shown in (b) along with the formula for $\vec{\delta q}$ and $\delta\omega$. (c) and (d) demonstrate the scattering processes with small and large $\delta\omega$ respectively. The former processes is forbidden, due to the lack of a final state which can satisfy the energy and momentum conservation laws. The threshold for $\delta\omega$ above which the scatterings are allowed is shown in Figs. (e)-(g) as a function of the momentum change δq , for a metal, topological semimetal and insulator accordingly.